Genuine compressibility effects in wall-bounded turbulence

Ming Yu and Chun-Xiao Xu
Key Laboratory of Applied Mechanics, Ministry of Education, Institute of Fluid Mechanics, and Department of Engineering Mechanics, Tsinghua University, Beijing 100084, China

Sergio Pirozzoli*
Dipartimento di Ingegneria Meccanica e Aerospaziale, Sapienza Università di Roma, and via Eudossiana 18, 00184 Rome, Italy

(Received 7 June 2019; published 5 December 2019)

Compressible wall-bounded turbulence is generally assumed to be devoid of genuine compressibility effects, meaning that the effect of finite fluid dilatation is regarded as "small," at least in the absence of disturbing pressure gradients. In the present paper we attempt to answer the basic question of how small these effects are, by interrogating a DNS database of compressible channel flow and by using Helmholtz decomposition to infer the relative magnitude and correlations between the solenoidal and the dilatational parts of turbulence velocity fields. Not surprisingly, we find dilatational velocity fluctuations to be much smaller than solenoidal ones, but perhaps unexpectedly, we find that finite correlation between the two components accounts for a nonnegligible fraction (about 10%) of the turbulent shear stress near walls, and for up to 4% of the wall skin friction. Quadrant analysis of the dilatational velocity fluctuations shows that the largest contribution to the turbulent shear stress results from significant correlation between positive streamwise solenoidal velocity fluctuations (i.e., high-speed streaks), and positive vertical dilatational velocity fluctuations, which tend to mitigate the intensity of wall-ward sweep events.

DOI: 10.1103/PhysRevFluids.4.123402

I. INTRODUCTION

Supersonic and hypersonic wall-bounded turbulence has been extensively studied for about a century, owing to its great technological importance in aerospace and mechanical engineering, most early studies having been carried out through experiments [1]. Direct numerical simulations (DNS) of compressible wall turbulence have become feasible in the past 30 years or so. Most studies have focused on representative canonical flow configurations, namely, the developed boundary layer over a flat plate [2–7] which is most relevant for obvious practical reasons, and the flow inside a planar channel [8–11], which is easier to study numerically owing to the presence of two directions of flow homogeneity.

All previous studies agree that, in the absence of disturbing elements such as shock waves, and/or imposed pressure gradients, compressibility effects mainly manifest themselves in the form of dependence of the statistical properties on the mean density and viscosity gradients. This is the essence of the classical Morkovin's hypothesis that owing to smallness of the fluctuating Mach number density fluctuations should be negligible [12]. This ansatz leads to several important consequences, such as the van Driest transformation for the mean velocity profile [13], and its generalizations [9,14,15]. General success of those compressibility transformations suggests that

*sergio.pirozzoli@uniroma1.it

Morkovin's hypothesis is quite solid, hence genuine compressibility effects due to finite fluid dilatation are regarded to be small, in general terms, although leading to obvious increase of pressure work and dilatational dissipation as the Mach number increases [4,10]. In particular, pressure work is dependent on the turbulence and gradient Mach number, as may be inferred from Green's function for pressure fluctuations [16], whereas dilatational dissipation depends on the turbulence Mach number and kurtosis [17,18]. The organization of coherent structures is also weakly affected by the Mach number, and for instance the spanwise spacing of velocity streaks slightly decreases as the free-stream Mach number increases [6,19]. At the same time, the streamwise length of the typical eddies decreases, and their inclination angle increases [4,20]. Shocklets induced by intense dilatational effects are observed when the fluctuating Mach number is high enough [4], but their volume fraction is small enough that no obvious contribution to overall flow structures results. This is consistent with the statement [21] that, although compressibility effects may be large in instantaneous flow fields, this is not necessarily reflected in the flow statistics.

Genuine compressibility effects in fluid flow may be generally characterized by exploiting Helmholtz decomposition of the velocity field into its solenoidal and dilatational constituents [22]. Helmholtz decomposition has been used in the analysis of compressible isotropic turbulence [23], and more recently for homogeneous shear flows [24]. In those studies it was found that energy and dissipation spectra, and two-point correlation of the solenoidal velocity field remain the same as in incompressible flow, even as the turbulence Mach number (M_t) approaches unity [25,26], whereas the dilatational part of the velocity field varies [24], with visible shocklets at $M_t \gtrsim 0.3$. The ratio of solenoidal to dilatational kinetic energy was found to scale as M_t^4 for $M_t \lesssim 0.1$, and as M_t^2 at higher M_t, attaining values as large as 0.22 as $M_t \approx 1$ [25], consistent with theoretical arguments [27]. To the best of our knowledge, Helmholtz decomposition has never been used for statistical analysis of wall-bounded flows.

The main goal of the present paper is to evaluate genuine compressibility effects in wall turbulence by mining a DNS database of canonical channel flow at various Mach numbers. To minimize complicating effects associated with abrupt variation of mean flow property near walls [28], a suitable internal cooling term is added to the governing equations. Helmholtz decomposition is then used to post-process the DNS results, thus allowing to quantify the effects of dilatational fluctuations on turbulent stresses and wall friction. The paper is organized as follows. In Sec. II we describe the physical model and its numerical implementation; in Sec. III we discuss basic statistics to characterize the turbulent flow in general terms; in Sec. IV we introduce the Helmholtz decomposition and show statistical moments and spectra of the solenoidal and dilatational velocity fields; in Sec. V we discuss dilatational contributions to skin friction, and in Sec. V A we identify the typical coherent structures responsible for the statistical observations. Concluding remarks are given in Sec. VI.

II. PHYSICAL AND NUMERICAL MODEL

We consider compressible turbulent flow in a planar channel with constant total mass and mass flux, and controllable temperature. Our intent is to replicate the flow of a fluid stream at Mach number M_0 coming from a long wind tunnel with constant wall temperature, equal to the recovery temperature in the upstream flow (see Fig. 1). We focus on the region of fully developed flow (dashed box), hence we consider streamwise and spanwise periodic boundary conditions. The mass and the mass flux are retained as at the nominal inflow, whereas the temperature needs to be adjusted, as the flow would otherwise heat up while progressing downstream owing to viscous friction. We consider the governing equations for a compressible ideal Newtonian gas. In a Cartesian coordinate system (x_i, $i = 1, 2, 3$, also referred to as x, y, z in the following) the Navier-Stokes equations read as

$$\frac{\partial \rho}{\partial t} + \frac{\partial \rho u_j}{\partial x_j} = 0, \tag{1}$$

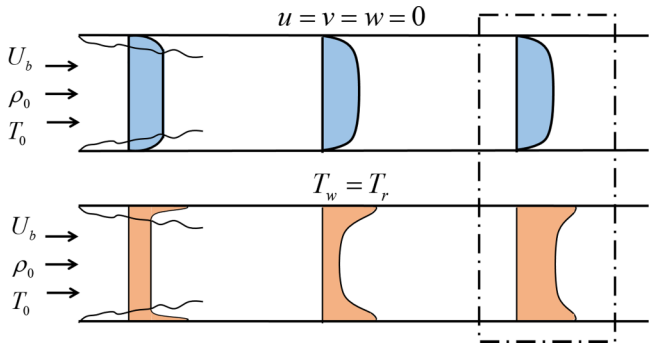

FIG. 1. Sketch of the flow configuration under scrutiny.

$$\frac{\partial \rho u_i}{\partial t} + \frac{\partial \rho u_i u_j}{\partial x_j} = -\frac{\partial p}{\partial x_i} + \frac{\partial \sigma_{ij}}{\partial x_j} + f_i \delta_{i1}, \tag{2}$$

$$\frac{\partial \rho E}{\partial t} + \frac{\partial \rho u_j E}{\partial x_j} = -\frac{\partial p u_j}{\partial x_j} + \frac{\partial u_i \sigma_{ij}}{\partial x_j} - \frac{\partial q_j}{\partial x_j} + f_1 u_1 - \phi, \tag{3}$$

with

$$\sigma_{ij} = 2\mu S_{ij} - \frac{2}{3}\mu S_{kk}\delta_{ij}, \quad q_j = -\lambda \frac{\partial T}{\partial x_j}, \quad E = e + \frac{1}{2}u_i u_i, \tag{4}$$

with μ and λ the dynamic viscosity and the heat conduction coefficient, and Pr (=0.71) the molecular Prandtl number. The variation of viscosity with temperature is accounted for through Sutherland's law. The ideal gas law is considered, namely, $p = \rho RT$ with R the gas constant, and the internal energy is obtained from $e = c_v T$, with c_v the constant-volume specific heat. As stated above, a body force f_1 and a cooling term ϕ are added to ensure constant mass flux and bulk temperature in the channel, the latter being set to

$$T_b = (1 - \alpha)T_0 + \alpha T_r, \tag{5}$$

where T_r is the estimated recovery temperature in the upstream boundary layer, $T_r = (1 + (\gamma - 1)\ r\ M_0^2/2)\ T_0$, with r the recovery factor, and the adjustable constant α controls the mean temperature gradient and the centerline Mach number. Periodic boundary conditions are applied in the streamwise (x) and spanwise (z) directions, and the nonslip condition for velocity and isothermal condition for temperature are applied at the upper and lower walls. The wall temperature is set to the nominal recovery value, $T(0) = T(2) = T_r$. Although the wall heat flux is not zero, as shown later it is small enough that its influence on the near-wall turbulence may be neglected. The bulk Reynolds number is defined as $\mathrm{Re}_b = \rho_0 U_b h/\mu_0$, and the bulk Mach number as $M_b = U_b/\sqrt{\gamma RT_b}$. An initially parabolic velocity profile is specified, $\langle u \rangle = 1.5U_b(y/h)(2 - y/h)$, along with uniform values of density and temperature, with added divergence-free sinuous perturbations [29]

$$u'(x, y, z) = f(y)\cos(k_z z), \quad w'(x, y, z)/U_b = f(y)\sin(k_x x), \tag{6}$$

with $k_x = 2/h$ and $k_z = 6/h$. The vertical distribution of the disturbances is controlled by function $f(y) = 8U_b(y/h)\exp[-100(y/h)^2]$, which attains a peak of 0.35 at $y/h = 0.07$ (corresponding to $y^+ \approx 40$ in the tests shown later).

As in incompressible flow, inner units are defined based on the friction velocity $u_\tau = (\langle \tau_w \rangle/\langle \rho_w \rangle)^{1/2}$, namely,

$$y^+ = \frac{\langle \rho_w \rangle y u_\tau}{\langle \mu_w \rangle}, \quad u^+ = \frac{\langle u \rangle}{u_\tau}, \tag{7}$$

TABLE I. Computational parameters for DNS flow cases. M_0 is the reference Mach number, Re_b is the bulk Reynolds number, α controls the mean internal energy [see Eq. (5)], Re_τ is the friction Reynolds number, M_b and M_c are the bulk and centerline Mach number, T_w is the wall temperature, Δx_i denotes the mesh spacing along the coordinate directions, and $-B_q = T_\tau/T_w$ is the heat flux parameter.

Case	M_0	Re_b	α	Re_τ	M_b	M_c	T_w/T_0	$\Delta x^+ \times \Delta z^+$	Δy^+	$-B_q$	Line style
C0	0.0	10032	–	550	–	–	1.0	10.0×6.7	$0.02 \sim 6.8$	–	◇
C1	0.8	10680	0.75	528	0.774	0.881	1.09	5.8×2.9	$0.61 \sim 8.5$	0.0043	
C2	1.5	13000	0.75	523	1.349	1.572	1.32	5.7×2.9	$0.60 \sim 7.4$	0.012	
C3	3.0	20000	0.75	496	2.151	2.529	2.28	5.4×2.8	$0.58 \sim 8.0$	0.028	
C4	6.0	42000	0.75	515	2.744	3.276	6.11	5.6×2.8	$0.59 \sim 8.2$	0.040	
C5	8.0	55000	0.75	494	2.879	3.484	10.09	5.4×2.7	$0.57 \sim 8.0$	0.044	
C6	8.0	80000	0.50	503	3.417	4.406	10.09	5.5×2.8	$0.65 \sim 9.1$	0.022	
C7	8.0	160000	0.25	504	4.444	6.970	10.09	5.5×2.7	$0.59 \sim 8.3$	0.015	

and hereafter denoted with the "+" subscript. The friction temperature is defined as

$$T_\tau = -\frac{\lambda \partial \langle T \rangle / \partial y|_w}{\langle \rho_w \rangle c_p u_\tau}, \tag{8}$$

and the friction Reynolds number as $\mathrm{Re}_\tau = h^+ = \langle \rho_w \rangle \langle u_\tau \rangle h/\mu_w$, where the w subscript indicates wall values. Ensemble averages of the generic variable φ are hereafter denoted as $\langle \varphi \rangle$, and the corresponding fluctuations as φ'. Favre averages, $\langle \rho\varphi \rangle / \langle \rho \rangle$, are denoted as $\widetilde{\varphi}$, and the corresponding fluctuation as φ''.

A modified version of the `Hoam-OPENCFD` code [30] is used to carry out the DNS. The governing equations are solved numerically by the finite-difference method described in Liang and Li [19], based on seventh-order upwind discretization of convective terms and sixth-order central discretization of viscous terms. A third-order TVD Runge-Kutta scheme is used for time advancement, and explicit filtering is further applied to ensure numerical stability at high Mach number [31].

The main parameters and numerical set-up of the DNS are listed in Table I. Case C0 is taken as a reference from the incompressible channel flow dataset of Bernardini *et al.* [32], with computational domain $6\pi h \times 2h \times 2\pi h$, and $1024 \times 256 \times 512$ grid points. In the compressible DNS flow cases C1–C7, the size of the computation domain is instead taken as $2\pi h \times 2h \times \pi h$ in streamwise, wall-normal and spanwise directions, respectively, with $576 \times 288 \times 576$ grid points, clustered in the wall-normal direction according to a hyperbolic tangent stretching function. To achieve similar friction Reynolds number in all cases, the bulk Reynolds number Re_b is adjusted along with the reference Mach number M_0, to compensate for temperature and viscosity variations. Compressibility effects are measured in terms of the bulk and centerline Mach numbers, which are significantly less than the reference value, owing to substantial increase of the wall temperature with M_0. The heat flux coefficient $-B_q = T_\tau/T_w$ is also reported, which as anticipated is found to be much smaller than in isothermal channels without a cooling term [11] (for $M_0 = 1.5$ we get $-B_q = 0.012$ compared to 0.072, and for $M_0 = 3$ we get $-B_q = 0.028$ compared to 0.14). The heat flux controlling parameter α is generally set to 0.75, however two extra cases with smaller α have also been carried out for $M_0 = 8$, to achieve higher M_b.

Grid resolution figures are provided in Table I, which are consistent with those reported in previous DNS studies of incompressible and compressible channels. Adequacy of the grid resolution was also tested a-posteriori by inspecting the velocity spectra, as shown in Fig. 2, in local Kolmogorov units. The figure shows general collapse of the spectra across flow cases and with reference incompressible data, with a common inertial behavior and flow-dependent roll-off past $k\eta \gtrsim 1$. We conclude that the grid is fine enough to accurately resolve all the energetically relevant

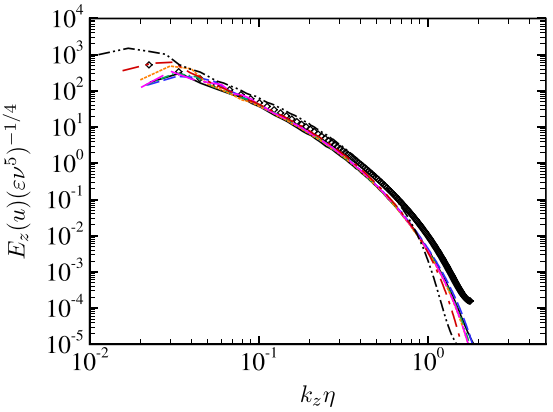

FIG. 2. Spanwise spectral densities of streamwise velocity fluctuations at $y/h = 0.3$, in local Kolmogorov units. Refer to Table I for line legend.

flow features. The flow statistics are averaged over one hundred time samples spaced $1.0h/U_b$ apart. We have checked that most results are converged with barely twenty samples. We have also monitored the time evolution of the solenoidal and dilatational energy, and verified that no drift occurs in the long term.

III. BASIC FLOW STATISTICS

The computed mean velocity and temperature profiles are shown in Fig. 3. As customary, the van Driest transformation is applied to the velocity profiles, namely,

$$u_{\mathrm{VD}} = \int_0^{\langle u \rangle} \sqrt{\langle \rho \rangle / \langle \rho_w \rangle}\, d\langle u \rangle. \tag{9}$$

Although other transformations may be more accurate in the presence of significant heat transfer [11,14], van Driest transformation works rather well here owing to the near-adiabatic wall conditions, and the transformed mean velocity profiles across different cases are fairly close to the standard incompressible log law for $y^+ \gtrsim 50$, although a systematic upward trend is observed with increasing Mach number. A tiny (if any) logarithmic layer is observed at this modest Reynolds

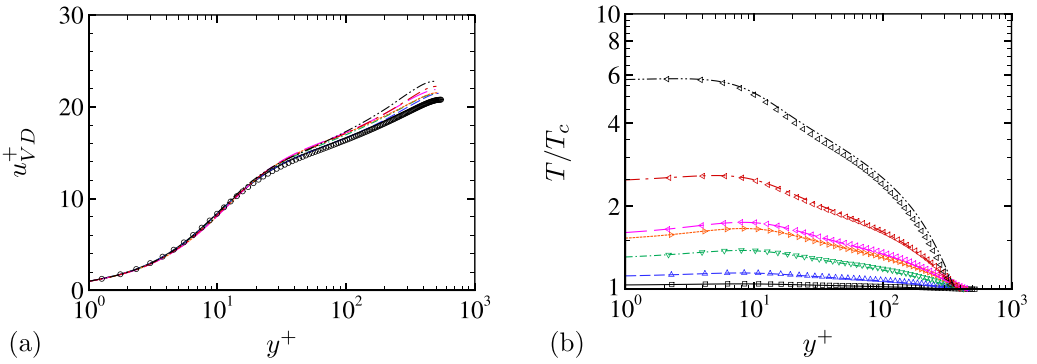

FIG. 3. Mean velocity (a) and temperature (b) profiles. T_c is the centerline temperature. Symbols in panel (b) indicate temperature profiles obtained from the GRA relationship in Equation 10. Refer to Table I for line legend.

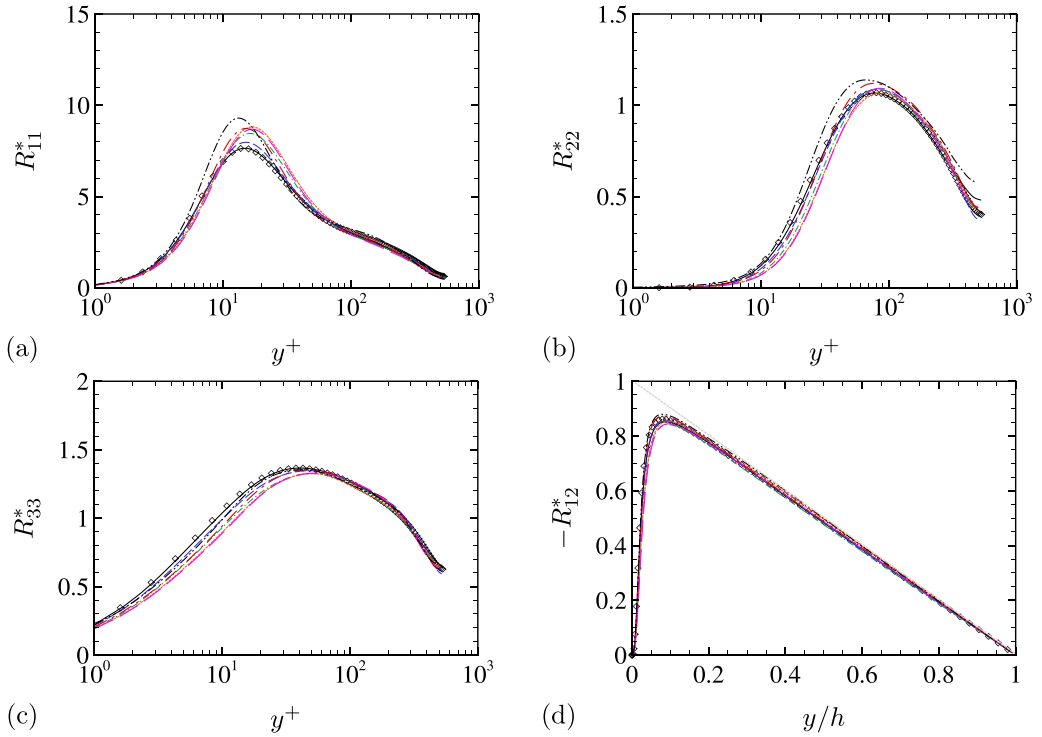

FIG. 4. Density-scaled Reynolds stresses distributions, as defined in Eq. (11). The gray line in (d) refers to the asymptotic shear stress distribution, $1 - y/h$. Refer to Table I for line legend.

number. The mean temperature profiles are shown in Fig. 3(b), along with predictions from the generalized Reynolds analogy (GRA) of Zhang *et al.* [33],

$$\langle T \rangle = T_w + \left(\langle u_c \rangle \frac{\partial \langle T \rangle}{\partial \langle u \rangle}\bigg|_w \right) \frac{\langle u \rangle}{\langle u_c \rangle} + \left(\langle T_c \rangle - T_w - \langle u_c \rangle \frac{\partial \langle T \rangle}{\partial \langle u \rangle}\bigg|_w \right) \frac{\langle u \rangle^2}{\langle u_c \rangle^2}, \tag{10}$$

where the subscript c refers to centerline properties. The mean temperature profiles very nearly coincide with the predicted distributions across the wall-distance range, suggesting that addition of a cooling term to the governing equations does not invalidate the GRA. It should be noted that increasing the cooling term through the parameter α yields stronger temperature gradients in the channel core, whereas the wall temperature gradients remain quite small in all cases.

The wall-normal distributions of the Reynolds stress components are shown in Fig. 4. As customary, density scaling is applied to the velocity fluctuations according to Morkovin's hypothesis. The resulting innerscaled distributions are denoted as

$$R_{ij}^* = \frac{\langle \rho \rangle \widetilde{u_i'' u_j''}}{\tau_w}, \tag{11}$$

where the diagonal components represent the velocity variances, and $-R_{12}^*$ is the turbulent shear stress. Good universality of the profiles is observed in the outer layer, whereas differences are found for $y^+ \lesssim 100$, especially regarding the streamwise fluctuations, Fig. 4(a), whose buffer-layer peak increases with the Mach number. However, the vertical and spanwise fluctuations slightly decrease with M_0, especially for $y^+ \lesssim 30$. Similar observations were previously made by Refs. [4,5]. The turbulent shear stress is shown in Fig. 4(d), where outer units are used for the vertical coordinate to better compare with the infinite-Reynolds number distribution $1 - y/h$, resulting from the mean

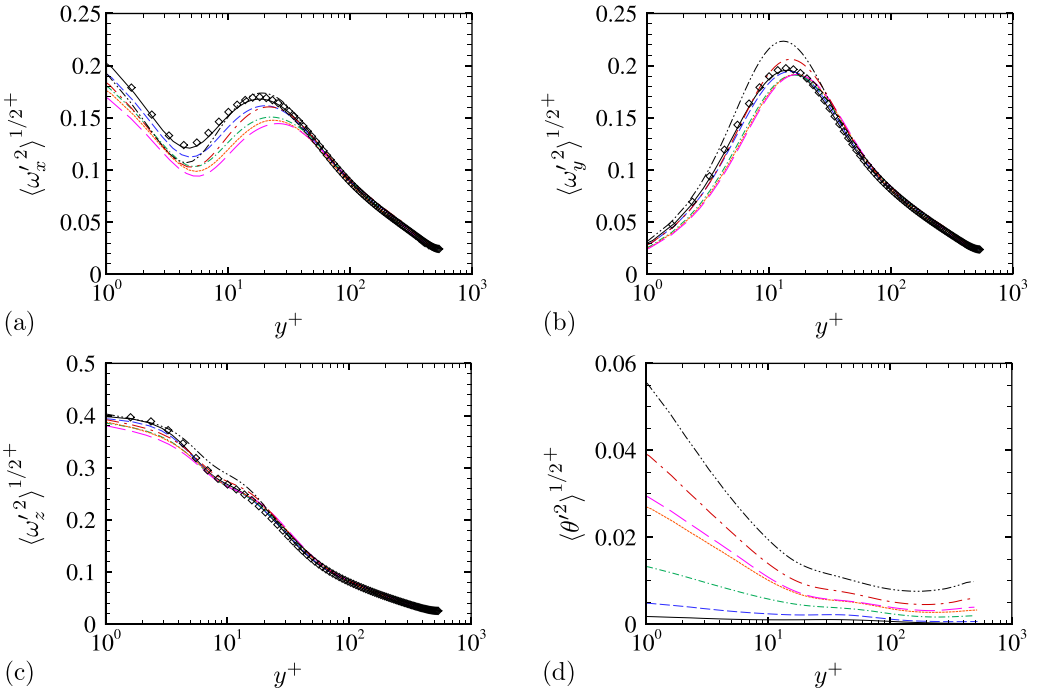

FIG. 5. Inner-scaled distributions of vorticity fluctuations (a)–(c), and dilatation fluctuations (d). Refer to Table I for line legend.

momentum balance. The results of the different flow cases are nearly indistinguishable, suggesting that Mach number influences on turbulent shear stress are globally small, for given friction Reynolds number.

The vorticity and divergence fluctuation intensities normalized in inner units (i.e., by τ_w/μ_w) are shown in Fig. 5. The streamwise vorticity fluctuation ω_x^+, which reflects the average strength of streamwise vortices (in idealized structural models), decreases with the Mach number below $y^+ = 30$ and collapse above logarithmic layer, which is consistent with the previous observation that cross-stream velocity fluctuations also decrease. The wall-normal and spanwise vorticity fluctuations, which are generally assumed to be associated with the average strength of velocity streaks and shear layers, respectively, collapse well across the y direction. The fluctuations of velocity dilatation, $\theta' = \boldsymbol{\nabla} \cdot \mathbf{u}'$, which reflect direct effects of compressibility, increase in amplitude with Mach number, as expected. Consistent with previous studies [8], maximum dilatational fluctuations are found at the wall, for reasons that will be clarified in the following. In any case, the magnitude is always much less than the vorticity fluctuations, as generally found in wall-bounded flows [4,34].

To bring out possible correlations between the dilatation field and the global flow organization, in Fig. 6 we show the correlation coefficients between dilatation fluctuations and velocity fluctuation components, defined as $C_{\theta u_i} = \langle \theta' u_i'' \rangle / (\langle \theta'^2 \rangle \langle u_i''^2 \rangle)^{1/2}$. The strongest correlation between θ and u (up to about 0.3) occurs in the buffer layer, where turbulence is most active. This points to nonnegligible statistical association between high-speed streaks and expansion (namely, $\theta' > 0$) zones, and/or between low-speed streaks and compressions ($\theta' < 0$). Strong positive correlation between θ and v instead occurs at the wall, whose peak value increases with the Mach number. This strong association is the results of kinematic constraints, as in the wall proximity $\theta' \sim \partial v''/\partial y \sim v''$, as a result of finite flow compressibility. Because of symmetry, the correlation coefficient $C_{\theta w}$ is nearly zero and not reported.

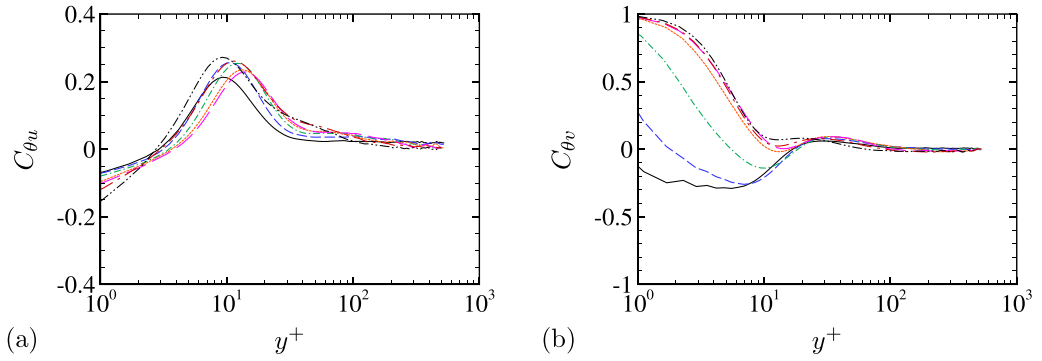

FIG. 6. Correlation coefficient between fluctuating dilatation and streamwise (a) and wall-normal (b) velocity fluctuations. Refer to Table I for line legend.

IV. COMPRESSIBILITY EFFECTS

The degree of compressibility in turbulent flow is traditionally measured in terms of either the turbulence Mach number ($M_t = \langle u_i'' u_i'' \rangle^{1/2} / \langle c \rangle$, with c the local sound speed), or the fluctuating Mach number (M', namely, the root-mean-square of the local Mach number), whose distributions are shown in Fig. 7. As expected, both M_t and M' increase with the bulk Mach number, although their behavior is quite different. Specifically, M_t attains its maximum in the buffer layer, basically following the same trend as the velocity variances (see Fig. 4). For reference, M_t for hypersonic boundary layer flow at $M_0 = 12$ from Duan *et al.* [4] is also shown in the figure. Higher values are found in the present channel-flow study, although the Mach number is not as high, presumably owing to large differences in the distribution of the speed of sound. Smits and Dussauge [35] pointed out that if M_t is locally higher than about 0.3, compressibility effects cannot be disregarded, which is the case here for some of the flow cases. The fluctuating Mach number also has a relative maximum in the buffer layer, which becomes a shoulder at the highest Mach numbers under study. Consistent with the findings of Duan *et al.* [4], an additional peak is found in the channel core, which becomes dominant at high M_0. Although weaker, the outer peak of M' resembles that observed in boundary layers, where it is associated with strong intermittency of the turbulent/nonturbulent interface (TNTI). Although no obvious TNTI is present in channels (however, see Ref. [36]), high values of M' are observed because of the strong temperature and density fluctuations in the core flow.

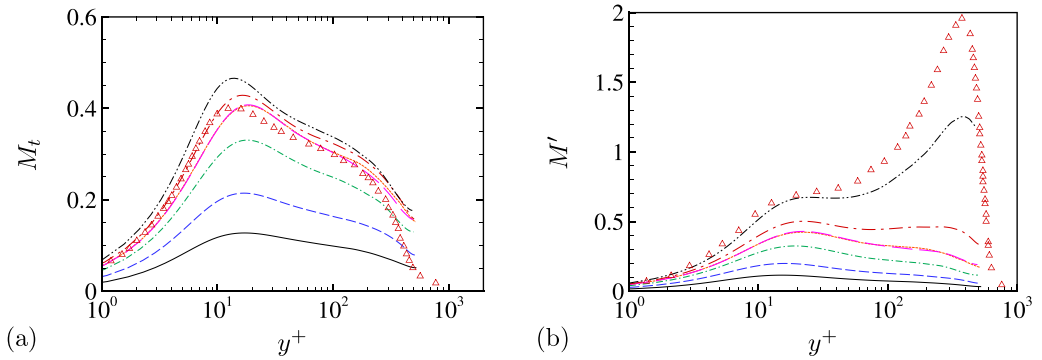

FIG. 7. Distributions of turbulence Mach number (a) and fluctuating Mach number (b). Refer to Table I for line legend. Symbols indicate boundary layer DNS data from Duan *et al.* [4].

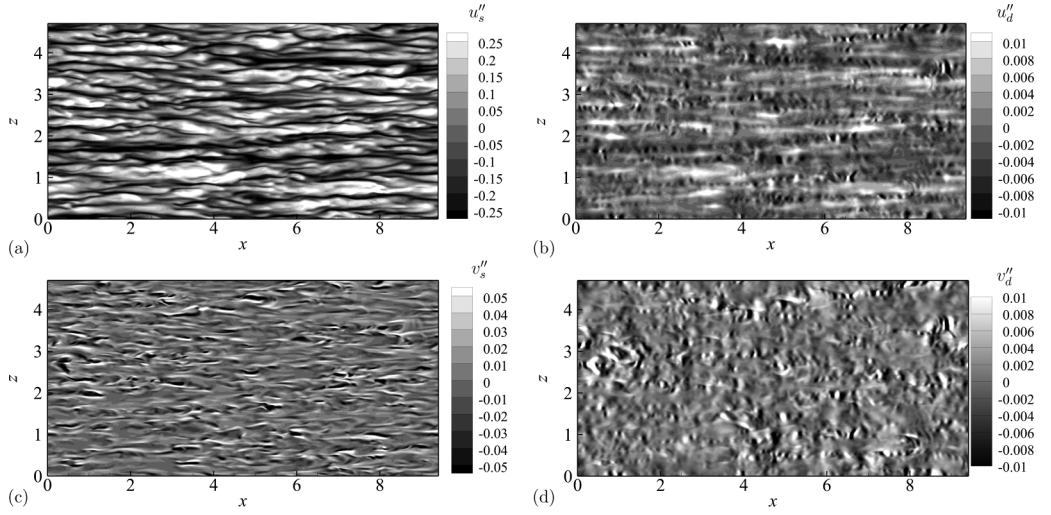

FIG. 8. Instantaneous fields of u_s'' (a), u_d'' (b), v_s'' (c), v_d'' (d), in a wall-parallel plane at $y^+ = 15$, for case C5.

As mentioned in the Introduction, Helmholtz decomposition has been frequently used to analyze isotropic and homogeneously sheared compressible turbulence, whereas application to wall-bounded turbulence seems to be lacking. In fact, Pirozzoli *et al.* [34] applied the Helmholtz decomposition to supersonic turbulent boundary layers to isolate the contributions of shear layers and vortex tubes to turbulence, however, disregarding compressibility effects. The essence of the Helmholtz decomposition is the attempt to cast the full velocity field as the sum of a vortical, solenoidal ($\mathbf{u}_s$) and a potential, dilatational ($\mathbf{u}_d$) component, satisfying, respectively, $\boldsymbol{\nabla} \cdot \mathbf{u}_s = 0$, $\boldsymbol{\nabla} \times \mathbf{u}_d = 0$. The two fields can be extracted from the velocity field $\mathbf{u}$ by solving Poisson equations for the vector potential $\mathbf{A}$ and for the velocity potential φ,

$$\nabla^2 \mathbf{A} = -\boldsymbol{\nabla} \times \mathbf{u}, \quad \nabla^2 \varphi = \boldsymbol{\nabla} \cdot \mathbf{u}, \tag{12}$$

whence $\mathbf{u}_d = \boldsymbol{\nabla}\varphi$ and $\mathbf{u}_s = \boldsymbol{\nabla} \times \mathbf{A}$ are obtained. Under the boundary conditions

$$\frac{\partial \varphi}{\partial y} = 0, \quad \frac{\partial A_y}{\partial y} = 0, \quad A_x = A_z = 0, \tag{13}$$

the vector potential is unique [37], and the gradient of φ is also unique. The Poisson Eqs. (12) are discretized spectrally in the periodic x and z directions, and by second-order central differences in the y direction. The algorithm has been extensively verified through tests on artificial flow fields, and it is applied to several three-dimensional flow samples to extract statistical information on $\mathbf{u}_s$ and $\mathbf{u}_d$.

The instantaneous decomposed velocity fields are shown in the buffer layer ($y^+ = 15$) in Fig. 8. The distinctive wall-turbulence streaky pattern is recovered for u_s, whereas vertical velocity fluctuations v_s have a more spotty appearance, resulting from ejection and sweep events. Clear association between the dilatational and solenoidal velocity fields is observed. Specifically, zones with positive u_d'' (white shades) clearly follow high-speed streaks. Negative u_s'' and u_d'' fluctuations are also clearly related. However, associated with low-speed streaks of u_s'' we find complex patterns of u_d'', consisting of alternating positive and negative fluctuations with small streamwise wavelength, probably interpretable as traveling wave packets. These traveling waves also contain vertical velocity fluctuations v_d'', which are found to be negatively correlated with v_s''. For the sake of statistical interpretation of the flow visualizations, we consider the following splitting of the

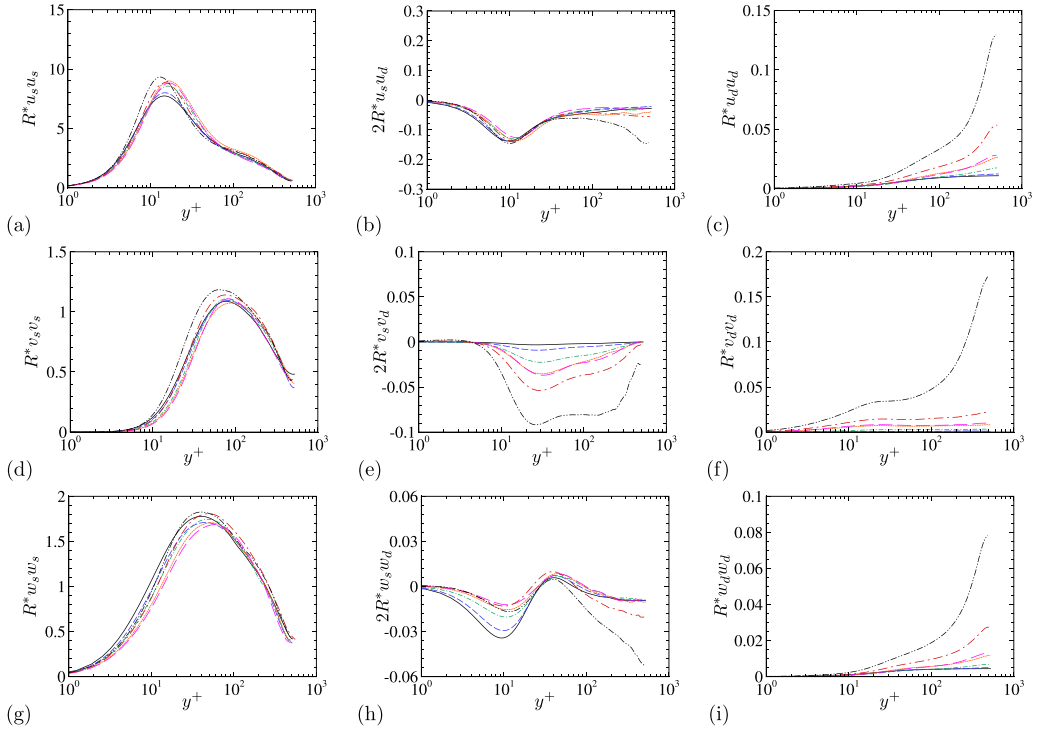

FIG. 9. Variance of solenoidal (a), (d), (g) and dilatational (c), (f), (i) velocity fluctuations, and their covariance (b), (e), (h). (a)–(c) u fluctuations, (d)–(f) v fluctuations, (g)–(i) w fluctuations. Refer to Table I for line legend.

Reynolds stresses,

$$R_{ij} = \langle\rho\rangle\widetilde{u_i''u_j''} = \langle\rho\rangle\widetilde{u_{i\,s}''u_{j\,s}''} + \langle\rho\rangle\widetilde{u_{i\,d}''u_{j\,d}''} + \langle\rho\rangle\widetilde{u_{i\,d}''u_{j\,s}''} + \langle\rho\rangle\widetilde{u_{i\,s}''u_{j\,d}''}. \tag{14}$$

We will refer to the first term at the right-hand side as solenoidal-solenoidal (SS), to the second term as dilatational-dilatational (DD), and to the third and fourth terms as solenoidal-dilatational (SD, DS), being, respectively, associated with the variance of the solenoidal and dilatational velocity fields, and with their covariance. The contributions to the diagonal Reynolds stress components are shown in Fig. 9, where as in Eq. (11), the star denotes density-weighted, inner-scaled quantities. The SS component clearly accounts for a prominent part of velocity fluctuations, for all flow cases. Notably, the fluctuation intensities of u_s'' and v_s'' are even higher than those of u'' and v'' (compare with Fig. 4), and a strong tendency to increase is observed for the buffer-layer peak of the u_s'' variance. The intensity of dilatational fluctuations is generally much smaller, although substantially increasing with the Mach number, and their trend is obviously similar to that previously noticed for the dilatation variance. Absolute maxima are attained at the channel centerline, where variances are about one tenth of the corresponding solenoidal velocity fluctuations. A notable exception to this scenario is provided by v_d'', whose variance is larger than v_s'' near the wall, at sufficiently high Mach number. This is due to their different asymptotic wall scaling, as $v_s'' \sim y^2$ as a results of incompressibility [38], whereas $v_d'' \sim y$ [21]. This is an important issue, implying that the largest effects of compressibility on the overall flow dynamics (if any) should be traced to the near-wall region. Unlike the case of homogeneously sheared turbulence [24], we find no evidence of simple parametrization of the dilatational to solenoidal kinetic energy with the turbulent or fluctuating Mach number, but rather we find (not shown) that the distributions tend to collapse when simply scaled by M_b^3. The covariance of dilatational and solenoidal velocity fluctuations is mainly confined

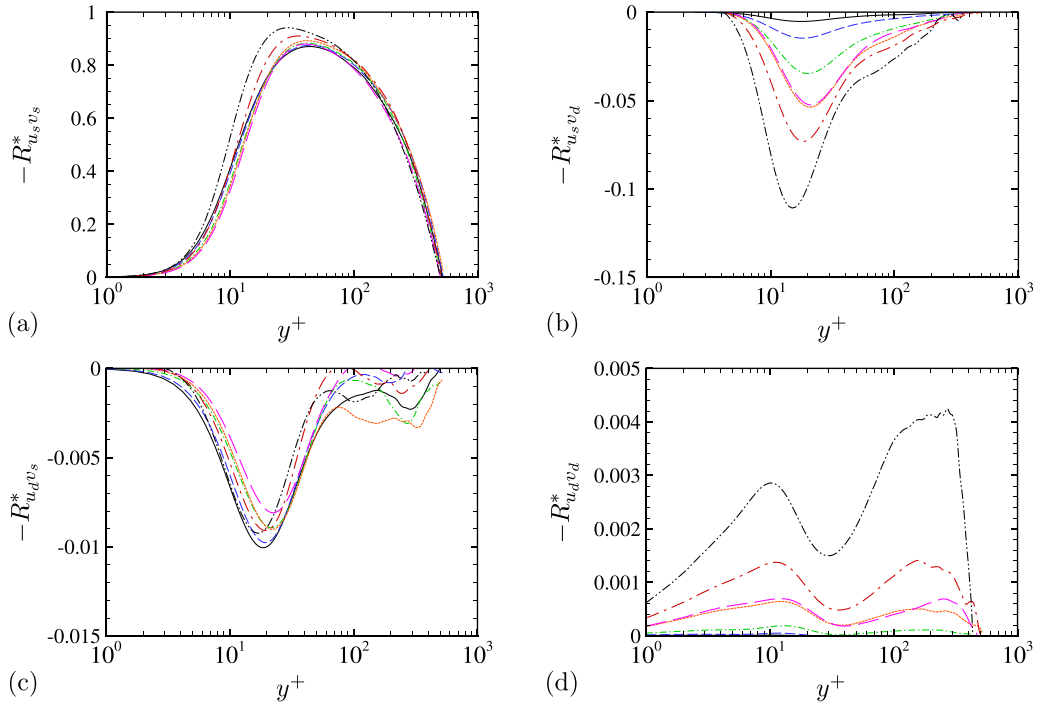

FIG. 10. Contributions to turbulent shear stress from (a) solenoidal velocity fluctuations (SS), (d) dilatational velocity fluctuations (DD), (b), (c) fluctuations covariances (SD and DS). Refer to Table I for line legend.

to the buffer layer, where it is larger than the variance of the dilatational fluctuations. Notably, the covariance of u_s'' and u_d'' is always negative, indicating that statistical correlation between the solenoidal and the dilatational velocity fields tends to compensate the increase of the solenoidal fluctuations intensity with the Mach number.

A separate analysis is carried out for the turbulent shear stress, in view of its direct relevance in the mean momentum budget, with subsequent impact on friction. From Eq. (14), four contributions may be identified, which are reported in Fig. 10. As expected, the SS component contributes most to the shear stress, and in fact it even overshoots the asymptotic $1 - y/h$ trend at high Mach number. The overshoot is compensated by the SD term [Fig. 10(b)], which is negative everywhere and clearly nonnegligible in the near-wall region. The DS term [Fig. 10(c)] is also negative, but an order of magnitude smaller. The direct compressibility term (DD) is increasing substantially with the Mach number, being negligible with respect to the other terms. For completeness of the analysis, in Fig. 11 we show the cross-correlation coefficients, $C_{u_s v_s}$ (associated with the SS contribution) and $C_{u_s v_d}$ (associated with the SD contribution). As typical of wall-bounded flows, the SS cross-correlation is close to 0.4 across large part of the channel [39]. However, the SD correlation is generally negative, and insensitive to Mach number variation. Hence, the increase of the magnitude of the SD terms observed in Fig. 10(b) is mainly due to the increase of the intensity of v_d' (recall Fig. 9).

Clear indication about the overall organization in wall-bounded flows is traditionally provided by the spectral maps of the velocity components (e.g., Ref. [40]). In Fig. 12 we thus show the spanwise spectra of the solenoidal and dilatational velocity fluctuations in pre-multiplied form, as a function of the respective wavelength. For the purpose of isolating the effect of scale variation from large inhomogeneity of the velocity variances across the wall layer (see Fig. 4), the spectra are presented in normalized form,

$$\hat{E}_\varphi(k_i) = E_\varphi(k_i)/\overline{\varphi'^2}, \tag{15}$$

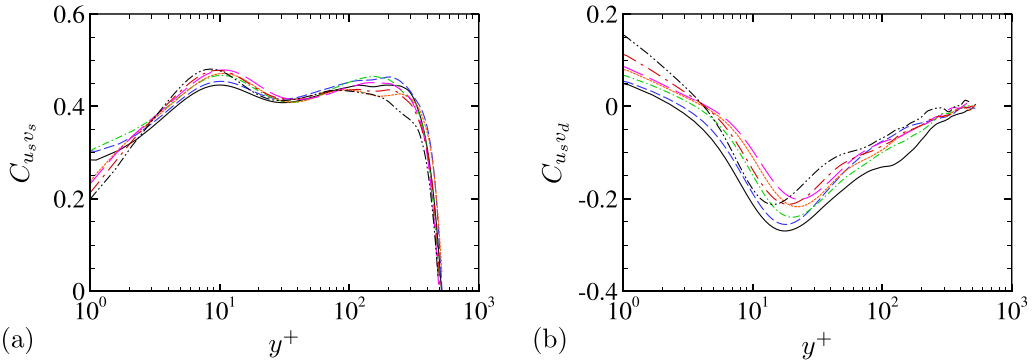

FIG. 11. Cross-correlation coefficients of horizontal and vertical decomposed velocity fluctuations. Refer to Table I for line legend.

where $E_\varphi(k_i)$ denotes the spectral density of variable φ in the ith coordinate direction, in such a way that they all integrate to unity at each y. The spectra of the solenoidal velocity field, shown in Figs. 12(a) and 12(b), have the same structure, irrespective of the Mach number. The same type of behavior is observed as in incompressible channel flow at moderate Mach number, with the distinctive buffer-layer signature consisting of a spectral peak at $\lambda_z^+ \approx 100$ for u_s, $\lambda_z^+ \approx 50$ for v_s, associated with near-wall streaks. A band of wall distances for which the typical length scale increases linearly is clearly visible in v_s, whereas u_s features a distinct outer energy site at $\lambda_z \approx h$, associated with outer-layer superstructures [41]. The spectra of the dilatational velocity components are shown in Figs. 12(c)–12(h). The streamwise dilatational velocity fluctuations [Figs. 12(c), 12(e), and 12(g)] are characterized by single typical length scale throughout the wall layer, $\lambda_z^+ \approx 100$. It is noteworthy that this is very similar to the length scale of the buffer-layer streaks, which probably points to a direct connection between the underlying hydrodynamic field and dilatational motions. More puzzling is the case of the vertical velocity fluctuations, which tend to be wider near the wall by a factor of about two, and which seem to have a similar spectral organization as u_s, with an outer spectral peak at $\lambda_z \approx h$. The reason for the largely different behavior of u_d and v_d is unclear at this stage.

V. DILATATIONAL CONTRIBUTIONS TO SKIN FRICTION

Given the previously noted nonnegligible contribution of dilatational velocity fluctuations to the turbulent shear stress, it is not surprising that they also contribute to the wall shear stress. To quantify that effect, we generalize the FIK identity [42], in its compressible flow extension [43], by decomposing the turbulent shear stress contributions. The starting point is the mean momentum balance, written in nondimensional form,

$$(1-y)\frac{C_f}{2} = -\langle\rho\rangle\widetilde{u''v''} + \frac{1}{\mathrm{Re}^\star}\left[(1+\langle\mu\rangle^\star)\frac{\partial u_{\mathrm{VD}}}{\partial y} + \left\langle\mu'^\star\left(\frac{\partial u'}{\partial y}+\frac{\partial v'}{\partial x}\right)\right\rangle\right], \tag{16}$$

where $\mathrm{Re}^\star = 2\rho_b U_b h/\langle\mu\rangle^\star$, $\langle\mu\rangle^\star = \mu_w - \langle\mu\rangle$, and $\mu'^\star = \mu'/\mu_w$. Integrating twice in y, one obtains

$$\frac{C_f}{2} = \underbrace{\frac{6}{\mathrm{Re}^\star}}_{C_V} \underbrace{-6\int_0^1 (1-y)\langle\rho\rangle\widetilde{u''v''}dy}_{C_T} + \underbrace{\frac{6}{\mathrm{Re}^\star}\int_0^1 (1-y)\langle\mu\rangle^\star\frac{\partial u_{\mathrm{VD}}}{\partial y}dy}_{C_M} + \underbrace{\frac{6}{\mathrm{Re}^\star}\int_0^1 (1-y)\left\langle\mu'^\star\left(\frac{\partial u'}{\partial y}+\frac{\partial v'}{\partial x}\right)\right\rangle dy}_{C_{M1}}, \tag{17}$$

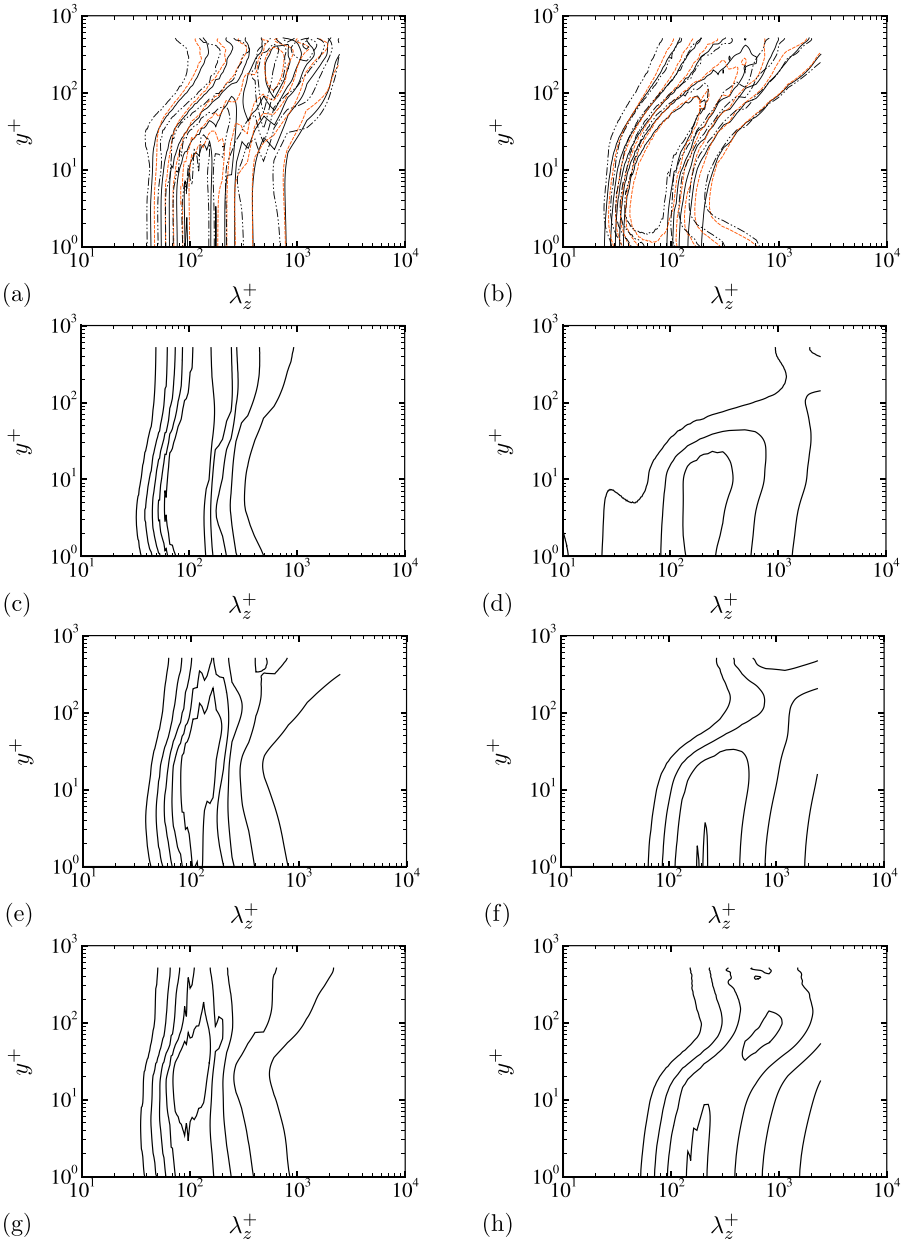

FIG. 12. Premultiplied normalized spanwise spectral densities $[k_z\hat{E}_\varphi(k_z)]$ of streamwise (left) and wall-normal (right) velocity fluctuations: $\varphi = u_s''$ (a), $\varphi = v_s''$ (b), $\varphi = u_d''$ (c), (e), (g), $\varphi = v_d''$ (d), (f), (h). Data are shown for all flow cases in panels (a), (b), line style as in Table I. Dilatational spectra are shown for flow cases C1 (c), (d), C4 (e), (f), C7 (g), (h). Contour levels from 0.1 to 0.5, in intervals of 0.1.

which reveals that mean skin friction is affected by the viscous term (C_V), turbulent shear stresses (C_T), mean viscosity variations (C_M), and turbulent viscosity fluctuations (C_{M1}). Substituting the

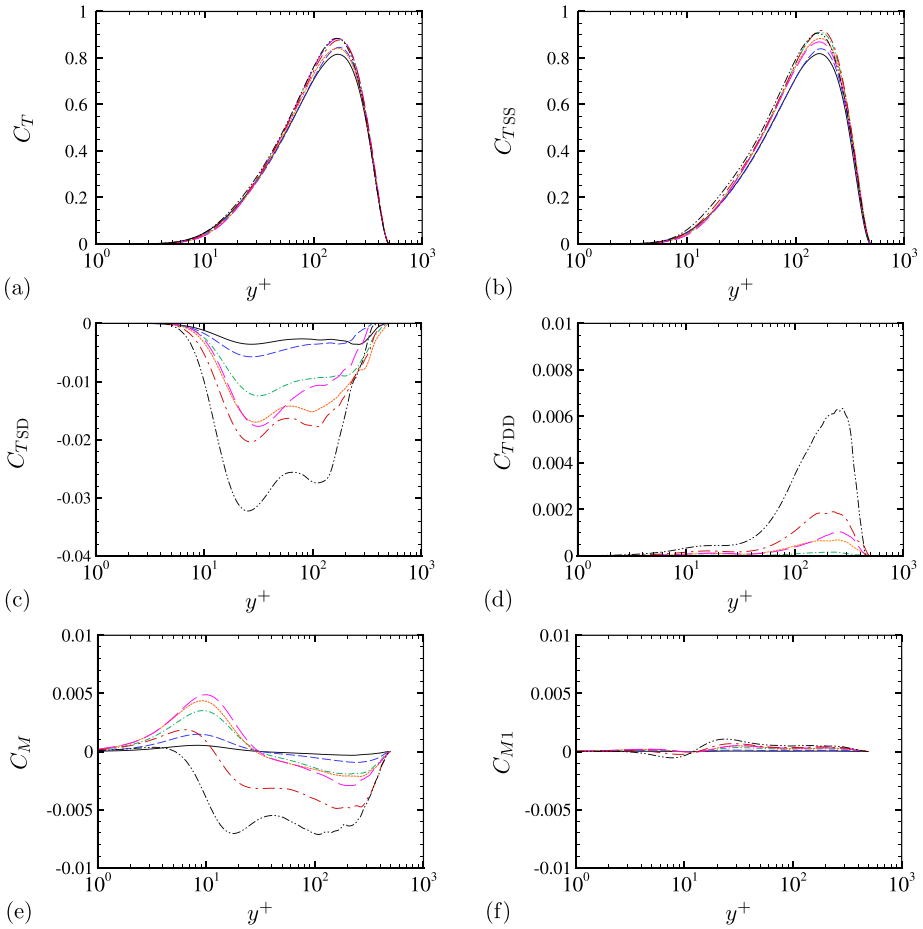

FIG. 13. Premultiplied integrands of terms contributing to mean wall friction from Eq. (18), normalized by $C_f/2$,: C_T (a), C_{TSS} (b), C_{TSD} (c), C_{TDD} (d), C_M (e), C_{M1} (f). Refer to Table I for line legend.

Reynolds stress decomposition Eq. (14) into Eq. (17) finally yields

$$\frac{C_f}{2} = \underbrace{\frac{6}{\mathrm{Re}^\star}}_{C_V} \underbrace{- 6\int_0^1 (1-y)\langle\rho\rangle\widetilde{u_s''v_s''}dy}_{C_{TSS}} \underbrace{- 6\int_0^1 (1-y)\langle\rho\rangle(\widetilde{u_s''v_d''} + \widetilde{u_d''v_s''})dy}_{C_{TSD}} \underbrace{- 6\int_0^1 (1-y)\langle\rho\rangle\widetilde{u_d''v_d''}dy}_{C_{TDD}}$$
$$+ \underbrace{\frac{6}{\mathrm{Re}^\star}\int_0^1 (1-y)\langle\mu\rangle^\star\frac{\partial u_{VD}}{\partial y}dy}_{C_M} + \underbrace{\frac{6}{\mathrm{Re}^\star}\int_0^1 (1-y)\left\langle\mu'^\star\left(\frac{\partial u''}{\partial y} + \frac{\partial v''}{\partial x}\right)\right\rangle dy}_{C_{M1}}. \tag{18}$$

Hence, the turbulent shear stress contribution is further split into the contribution from solenoidal velocity fluctuations (C_{TSS}), from dilatational velocity fluctuations (C_{TDD}), and from their cross-correlation (C_{TSD}). The premultiplied integrands corresponding to these terms are shown in Fig. 13. The turbulent solenoidal contribution is clearly dominant over the other ones, being distributed across the wall layer, and receiving large contribution from the logarithmic layer. The turbulent dilatational contribution is much smaller, and it also exhibits a secondary peak in the buffer layer. It is noteworthy that the term associated with solenoidal/dilatational correlations is not negligible, and it attains a negative peak in the buffer layer, which increases in magnitude with M_b. The

TABLE II. Mean friction coefficient (C_f) and integrated contributions of terms in Eq. (18) as percentage of the total.

Case	$C_f(\times 10^3)$	C_V	C_T	$C_{T\,\mathrm{SS}}$	$C_{T\,\mathrm{DD}}$	$C_{T\,\mathrm{SD}}$	C_M	C_{M1}
C0	5.91	10.22%	89.78%	–	–	–	–	–
C1	5.76	10.49%	89.49%	89.42%	−0.0003%	−0.577%	0.0214%	0.0077%
C2	5.32	10.50%	89.45%	89.62%	0.0002%	−0.737%	0.0555%	0.0208%
C3	4.70	11.35%	88.53%	91.39%	0.0122%	−1.64%	0.119%	0.0483%
C4	4.17	11.16%	88.68%	93.84%	0.0609%	−2.38%	0.160%	0.0646%
C5	3.91	11.69%	88.15%	88.25%	0.0597%	−1.92%	0.162%	0.0660%
C6	2.89	10.93%	89.55%	94.11%	0.153%	−2.72%	−0.488%	0.0697%
C7	1.51	10.61%	90.53%	95.13%	0.482%	−3.77%	−1.143%	0.0856%

terms associated with mean viscosity variation have roughly the same order of magnitude, but they are more concentrated toward the wall, and also increasing with M_b, whereas terms due to viscosity fluctuations are very small. The integrated fractional contributions of the various terms to skin friction are listed in Table II. At the moderate Reynolds numbers under scrutiny, viscosity yields a nonnegligible contribution to friction of about 10%. The turbulent shear stress accounts for approximately the remaining 90% of the skin friction, this percentage being weakly affected by Mach number. Within this large percentage, we find a competitive effect of solenoidal turbulent stresses which would tend to increase C_f, and of stresses resulting from solenoidal/dilatational correlations, which instead tend to decrease it, yielding a negative net effect which increases very nearly linearly with M_b, up to 4%.

A. Coherent structures

As previously pointed out, the flow is characterized by significant correlation between streamwise solenoidal velocity fluctuations and vertical dilatational velocity fluctuations. Traditionally, the statistical association of horizontal and vertical velocity fluctuations is studied through their joint probability function, referred to as quadrant analysis [44]. The quadrant analysis of the decomposed Reynolds stress of C1, C4, and C7 cases is reported in Fig. 14, at $y^+ = 20$. Similar to the case of incompressible wall turbulence, the joint probability density function (p.d.f.) of the solenoidal velocity components (u_s, v_s) shows dominance of second- and fourth-quadrant events, the latter being statistically more frequent and the former more intense. The joint p.d.f. of the dilatational velocity field, (u_d, v_d), shows large negative skewness of the horizontal fluctuations, with strong negative u_d'' events, but no significant correlation with vertical fluctuations. The SD (u_s, v_d) joint p.d.f. shows no evidence of correlation for negative u_s'' events, namely, low-speed streaks, however it shows that the most frequent events, which have small positive u_s'' and positive v_d'', tend to be positively correlated. The DS (u_d, v_s) joint p.d.f. also shows some positive correlation between horizontal and vertical velocity fluctuations, with second and fourth quadrants relatively depleted of events.

In view of the much larger effect of the SD cross-correlation on the turbulent shear stress (recalling Fig. 10) with respect to other dilatational effects, (u_s, v_d) events are further scrutinized to determine the typical associated eddies. For that purpose, we evaluate the statistical averages of the DNS flow fields based on the condition

$$\overline{\varphi}(\Delta x, y, \Delta z) = \langle \varphi(x + \Delta x, y, z + \Delta z) | u_s''(x, y_{\mathrm{ref}}, z) > 0, v_d''(x, y_{\mathrm{ref}}, z) > 0, u_s'' v_d'' > \left(\overline{u_s''^2}\,\overline{v_d''^2}\right)^{1/2} \rangle. \tag{19}$$

The analysis is then restricted to strong first-quadrant events, which based on the analysis of the covariance integrands (not shown) are found to yield larger contribution to the covariance. The resulting vortical structures and dilatation fields are shown in Fig. 15, superposed to the conditional

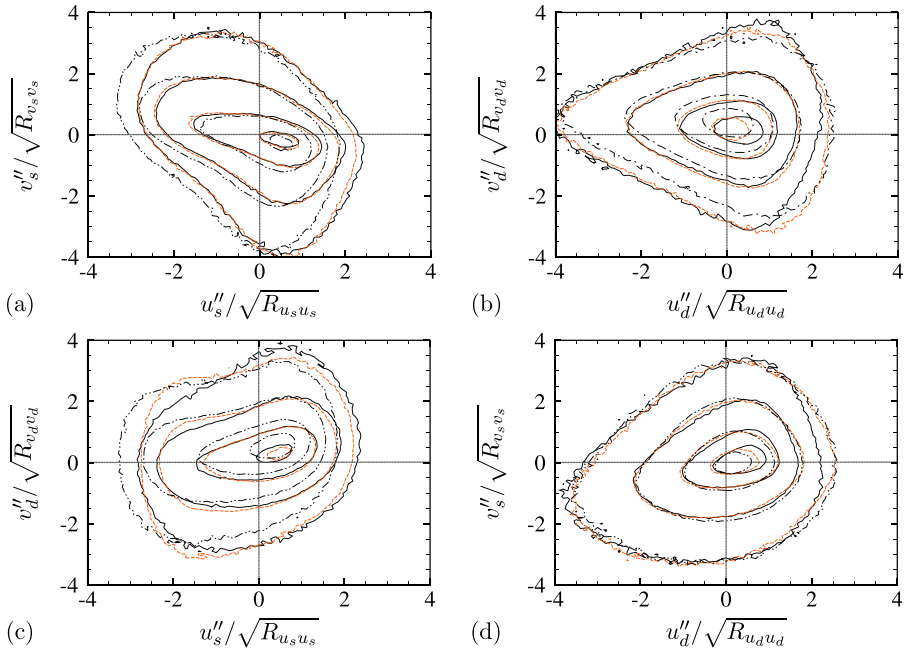

FIG. 14. Quadrant analysis of solenoidal and dilatational velocity fluctuations [(a), SS (u_s, v_s); (b), DD (u_d, v_d); (c) SD (u_s, v_d); (d), DS (u_d, v_s)], at $y^+ = 20$ for flow cases C1, C4, and C7 (refer to Table I for line legend). The contour levels 0.002, 0.02, 0.1, and 0.2, are shown.

velocity field in the reference plane, taken in the buffer layer. Following Zhou *et al.* [45], we identify vortical structures based on the swirling strength (λ_{ci}), namely, the imaginary part of the complex eigenvalue pair of the conditional velocity gradient tensor. The topology of the educed eddies consists of a pair of quasistreamwise legs, forming a small angle with respect to the wall plane, connected upstream by a quasispanwise head. Based on the sign of the streamwise vorticity used to color the swirling strength isosurface, we may interpret those eddies as retrograde hairpins (namely, whose spanwise vorticity has opposite sign to the mean [46]), pumping high-speed fluid toward the wall between their legs, hence linked with sweep events and high-speed streaks. We find that these events are associated with positive dilatation patches underneath, namely, expansions with positive v_d''. This is consistent with the above noted positive correlation of u_s and v_d, and it physically points to the fact that finite flow compressibility tends to oppose wall-ward motions, thus limiting the strength of sweep events, and also limiting turbulent shear stress in the buffer layer. A similar, but reverse behavior is observed in conditional events based on negative u_s'', hence on low-speed streaks, which instead yield prograde hairpins as typical structures, inducing negative dilatation between their legs. Again, based on the previous quadrant analysis, they convey much smaller contribution to the overall turbulent shear stress, hence the related conditional flow patterns are not shown.

VI. CONCLUSION

We have carried out a numerical study of compressible turbulent channel flow, in a set-up which allows for weak variation of the mean thermodynamic properties. The latter are regarded to be responsible for what are generally referred to as compressibility effects, which is the reason why transformations based on the mean density and viscosity gradients are rather successful in mapping compressible results onto incompressible data. In this study we have rather focused on

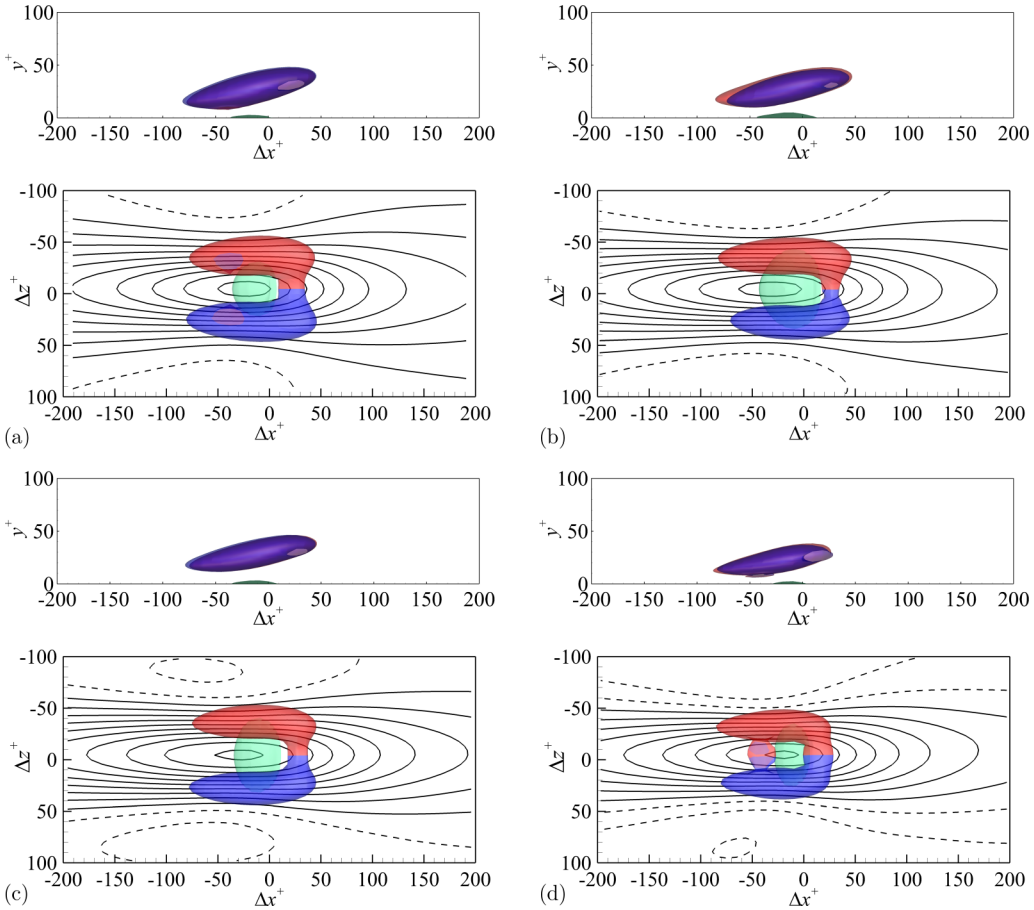

FIG. 15. Conditional average eddies based on condition Eq. (19) for flow case C1 (a), C3 (b), C5 (c), and C7 (d). Isosurfaces of $\lambda_{ci} = 0.6$ are shown colored in red and blue (corresponding to positive and negative ω_x, respectively), overlaid to isosurfaces of dilatation, in green (a, $\theta = 0.03$; b, $\theta = 0.15$; c, $\theta = 0.3$; d, $\theta = 0.6$). Streamwise velocity contours at the conditioning wall distance ($y^+_{ref} = 20$) are also shown (levels from -0.19 to 0.19 in intervals of 0.02: solid, positive; dashed, negative).

the genuine effects of flow compressibility, related to finite dilatation of the fluid. For that purpose, the Helmholtz decomposition has been used, which allows to effectively separate the dilatational velocity fluctuations from the underlying vortical, hydrodynamic field. Bulk Mach numbers up to $M_b \approx 4.4$ are included in the database, which yield moderate turbulent Mach numbers up to $M_t \approx 0.45$. Under these conditions, we find that the fraction of dilatational kinetic energy to the solenoidal kinetic energy is less than 1% in the buffer layer, increasing to about 10% toward the channel centerline, where potential velocity fluctuations are relatively most intense. Notably, this fraction is found to increase as M_b^3, which allows for extrapolation of the present results to more extreme flow conditions. Also important is the fact that, because of violation of the divergence-free conditions, dilatational vertical velocity fluctuations in the viscous sublayer may be larger than the solenoidal ones, which allows for some dynamical near-wall effect. In fact, we find nonnegligible statistical association between high-speed streaks and vertical dilatational velocity fluctuations, which affects the turbulent shear stress by as much as 10% within the buffer layer. As a consequence of the contribution to the turbulent shear stress, we find that dilatational effects also contribute to mean friction. In fact, use of a modified FIK identity shows that dilatational effects yield a nominal

decrease (with respect to the purely incompressible case) of about 4% at the highest Mach number considered, a fraction which is found to increase about linearly with M_b. Given the nonnegligible dynamical relevance of dilatational motions in the buffer layer, we have also carried out an analysis of the typical associated coherent structures by taking conditional averaged of the DNS flow fields. Consistent with previously advocated kinematic arguments, we find that most dilatational effects are concentrated in the viscous sublayer, corresponding to expansion regions which tend to counteract wall-ward motions associated with hydrodynamic sweep events. We have also studied the spatial organization of dilatational motions away from walls, and characterized their typical size through spectral maps. Some issues remain puzzling, for instance the noted different behavior of dilatational motions near high- and low-speed streaks, with the latter featuring streamwise-aligned alternating expansion and compression bands, resembling wave packets. It should finally be noted that the results herein presented strictly pertain to the case of nearly adiabatic walls, but the conclusions might in principle change in the presence of significantly heated or cooled walls. These and other topics are left for future studies.

ACKNOWLEDGMENTS

The authors acknowledge financial support from the National Natural Science Foundation of China (Grant No. 91752205) and the National Key Research and Development Program of China (Grant No. 2016YFA0401200).

[1] E. F. Spina, A. J. Smits, and S. K. Robinson, The physics of supersonic turbulent boundary-layers, Annu. Rev. Fluid Mech. **26**, 287 (1994).
[2] S. Pirozzoli, F. Grasso, and T. B. Gatski, Direct numerical simulation and analysis of a spatially evolving supersonic turbulent boundary layer at $M = 2.25$, Phys. Fluids **16**, 530 (2004).
[3] L. Duan, I. Beekman, and M. P. Martin, Direct numerical simulation of hypersonic turbulent boundary layers. Part 2. Effect of wall temperature, J. Fluid Mech. **655**, 419 (2010).
[4] L. Duan, I. Beekman, and M. P. Martin, Direct numerical simulation of hypersonic turbulent boundary layers. Part 3. Effect of Mach number, J. Fluid Mech. **672**, 245 (2011).
[5] M. Lagha, J. Kim, J. D. Eldredge, and X. Zhong, A numerical study of compressible turbulent boundary layers, Phys. Fluids **23**, 015106 (2011).
[6] S. Pirozzoli and M. Bernardini, Turbulence in supersonic boundary layers at moderate Reynolds number, J. Fluid Mech. **688**, 120 (2011).
[7] M. F. Shahab, G. Lehnasch, T. B. Gatski, and P. Comte, Statistical characteristics of an isothermal, supersonic developing boundary layer flow from DNS data, Flow Turbul. Combust. **86**, 369 (2011).
[8] G. N. Coleman, J. Kim, and R. D. Moser, A numerical study of turbulent supersonic isothermal-wall channel flow, J. Fluid Mech. **305**, 159 (1995).
[9] P. G. Huang, G. N. Coleman, and P. Bradshaw, Compressible turbulent channel flows: DNS results and modelling, J. Fluid Mech. **305**, 185 (1995).
[10] H. Foysi, S. Sarkar, and R. Friedrich, Compressibility effects and turbulence scalings in supersonic channel flow, J. Fluid Mech. **509**, 207 (2004).
[11] D. Modesti and S. Pirozzoli, Reynolds and Mach number effects in compressible turbulent channel flow, Int. J. Heat Fluid Flow **59**, 33 (2016).
[12] M. V. Morkovin, *Effects of Compressibility on Turbulent Flows* (CNRS, Paris, 1962), p. 380.
[13] E. R. Van Driest, Turbulent boundary layer in compressible fluids, J. Aero. Sci. **18**, 145 (1951).
[14] A. Trettel and J. Larsson, Mean velocity scaling for compressible wall turbulence with heat transfer, Phys. Fluids **28**, 026102 (2016).
[15] A. Patel, B. J. Boersma, and R. Pecnik, The influence of near-wall density and viscosity gradients on turbulence in channel flows, J. Fluid Mech. **809**, 793 (2016).

[16] W. D. Thacker, S. Sarkar, and T. B. Gatski, Analyzing the influence of compressibility on the rapid pressure-strain rate correlation in turbulent shear flows, Theor. Comput. Fluid Dyn. **21**, 171 (2007).
[17] O. Zeman, Dilatation dissipation: The concept and application in modeling compressible mixing layers, Phys. Fluids A **2**, 178 (1990).
[18] J. Kreuzinger, R. Friedrich, and T. B. Gatski, Compressibility effects in the solenoidal dissipation rate equation: *A priori* assessment and modeling, Int. J. Heat Fluid Flow **27**, 696 (2006).
[19] X. Liang and X. Li, Direct numerical simulation on Mach number and wall temperature effects in the turbulent flows of flat-plate boundary layer, Commun. Comput. Phys. **17**, 189 (2015).
[20] S. Pirozzoli, M. Bernardini, and F. Grasso, Characterization of coherent vortical structures in a supersonic turbulent boundary layer, J. Fluid Mech. **613**, 205 (2008).
[21] T. B. Gatski and J. P. Bonnet, *Compressibility, Turbulence and High Speed Flow* (Academic Press, San Diego, CA, 2013).
[22] P. Sagaut and C. Cambon, *Homogeneous Turbulence Dynamics*, Vol. 10 (Springer, Berlin, 2008).
[23] R. Samtaney, D. I. Pullin, and B. Kosović, Direct numerical simulation of decaying compressible turbulence and shocklet statistics, Phys. Fluids **13**, 1415 (2001).
[24] S. Chen, J. Wang, H. Li, M. Wan, and S. Chen, Spectra and Mach number scaling in compressible homogeneous shear turbulence, Phys. Fluids **30**, 065109 (2018).
[25] J. Wang, Y. Shi, L. P. Wang, Z. Xiao, X. He, and S. Chen, Effect of shocklets on the velocity gradients in highly compressible isotropic turbulence, Phys. Fluids **23**, 125103 (2011).
[26] J. Wang, Y. Shi, L. P. Wang, Z. Xiao, X. T. He, and S. Chen, Effect of compressibility on the small-scale structures in isotropic turbulence, J. Fluid Mech. **713**, 588 (2012).
[27] J. R. Ristorcelli, A pseudo-sound constitutive relationship for the dilatational covariances in compressible turbulence, J. Fluid Mech. **347**, 37 (1997).
[28] Y. Morinishi, S. Tamano, and K. Nakabayashi, Direct numerical simulation of compressible turbulent channel flow between adiabatic and isothermal walls, J. Fluid Mech. **502**, 273 (2004).
[29] W. Schoppa and F. Hussain, Coherent structure generation in near-wall turbulence, J. fluid Mech. **453**, 57 (2002).
[30] X. Li, D. Fu, and Y. Ma, Direct numerical simulation of hypersonic boundary layer transition over a blunt cone, AIAA J. **46**, 2899 (2008).
[31] X. Li, D. X. Fu, and Y. W. Ma, Direct numerical simulation of a spatially evolving supersonic turbulent boundary layer at $\mathrm{Ma} = 6$, Chin. Phys. Lett. **23**, 1519 (2006).
[32] M. Bernardini, S. Pirozzoli, and P. Orlandi, Velocity statistics in turbulent channel flow up to $\mathrm{Re}_\tau = 4000$, J. Fluid Mech. **742**, 171 (2014).
[33] Y. S. Zhang, W. T. Bi, F. Hussain, and Z. S. She, A generalized Reynolds analogy for compressible wall-bounded turbulent flows, J. Fluid Mech. **739**, 392 (2014).
[34] S. Pirozzoli, M. Bernardini, and F. Grasso, On the dynamical relevance of coherent vortical structures in turbulent boundary layers, J. Fluid Mech. **648**, 325 (2010).
[35] A. J. Smits and J. P. Dussauge, *Turbulent Shear Layers in Supersonic Flow* (Springer, Berlin, 2006).
[36] Y. S. Kwon, J. Philip, C. M. de Silva, N. Hutchins, and J. P. Monty, The quiescent core of turbulent channel flow, J. Fluid Mech. **751**, 228 (2014).
[37] G. J. Hirasaki and J. D. Hellums, Boundary conditions on the vector and scalar potentials in viscous three-dimensional hydrodynamics, Qu. App. Math. **28**, 293 (1970).
[38] A. A. Townsend, *The Structure of Turbulent Shear Flow* (Cambridge University Press, Cambridge, 1976).
[39] P. J. A. Priyadarshana and J. C. Klewicki, Study of the motions contributing to the Reynolds stress in high and low Reynolds number turbulent boundary layers, Phys. Fluids **16**, 4586 (2004).
[40] J. C. del Álamo, J. Jiménez, P. Zandonade, and R. D. Moser, Scaling of the energy spectra of turbulent channels, J. Fluid Mech. **500**, 135 (2004).
[41] N. Hutchins and I. Marusic, Evidence of very long meandering features in the logarithmic region of turbulent boundary layers, J. Fluid Mech. **579**, 1 (2007).
[42] K. Fukagata, K. Iwamoto, and N. Kasagi, Contribution of Reynolds stress distribution to the skin friction in wall-bounded flows, Phys. Fluids **14**, L73 (2002).

[43] T. Gomez, V. Flutet, and P. Sagaut, Contribution of Reynolds stress distribution to the skin friction in compressible turbulent channel flows, Phys. Rev. E **79**, 035301(R) (2009).
[44] J. M. Wallace, Quadrant analysis in turbulence research: History and evolution, Annu. Rev. Fluid Mech. **48**, 131 (2016).
[45] J. Zhou, R. J. Adrian, S. Balachandar, and T. M. Kendall, Mechanisms for generating coherent packets of hairpin vortices in channel flow, J. Fluid Mech. **387**, 353 (1999).
[46] V. K. Natrajan, Y. Wu, and K. T. Christensen, Spatial signatures of retrograde spanwise vortices in wall turbulence, J. Fluid Mech. **574**, 155 (2007).